Influence of Solidity on the Performance of a Cross-Flow Turbine

C.A. Consul, R.H.J Willden, E. Ferrer, M.D. McCulloch

Department of Engineering Science
University of Oxford
Parks Road, OX1 3PJ, Oxford, UK
Email: `claudio.consul@eng.ox.ac.uk`

Abstract

This paper presents a numerical investigation of the influence of solidity on the hydrodynamics of a generic tidal cross-flow turbine. Flows through two- and four-bladed turbines were simulated at a high laboratory Reynolds number, $O(10^5)$. The corresponding turbine solidities were 0.019 and 0.038.

It was found that increasing the number of blades led to an increase in the maximum power coefficient from 0.43 to 0.53. Furthermore, the power curve shifted to a lower range of tip speed ratios due to an increase in flow impedance, and hence reduced streamwise flow velocity, that resulted from the higher turbine solidity.

It was observed that dynamic stall occurred at the lowest tip speed ratios. However, its net effect on turbine performance was found to be negative.

Keywords: Hydrodynamics, Tidal Stream Turbine, Cross-Flow Turbine, Computational Fluid Dynamics, Dynamic Stall

Nomenclature

Re	=	Reynolds number
c	=	Chord length
λ	=	Tip speed ratio
α	=	Angle of attack
α_{ss}	=	Static stalling angle
θ	=	Azimuth angle
$C_{L,D,P}$	=	Coefficient of lift, drag and power
$U_{r,\infty,\theta}$	=	Resultant, free-stream and blade rotational velocity
$U_{x,y}$	=	Streamwise and cross-stream velocity components
ω	=	Angular Velocity
β	=	Streamwise velocity induction factor
ρ	=	Fluid density
ν	=	Kinematic viscosity
y^+	=	Wall normal distance
τ_ω	=	Wall shear stress
σ	=	Turbine solidity
B	=	Number of blades
R	=	Turbine radius
T	=	Torque per unit length of blade
A	=	Projected frontal area of the turbine per unit length of blade
L	=	Blade sectional lift
D	=	Blade sectional drag

1 Introduction

The urgent need to establish a clean, safe and affordable energy supply has placed increased emphasis on the exploitation of new renewable energy sources. The ocean offers immense potential for clean energy extraction and, besides wave power and tidal barrage technologies, tidal stream turbines have been identified as prospective marine energy converters. The extractable energy potential due to tidal streams around the British Isles is estimated to be 18 TWh/y [1], which equates to 5% of the UK's energy consumption in 2008 [2]. However, this resource has not yet been exploited and as the underlying flow physics of tidal turbines is not fully understood, fundamental research is still required to ensure tidal energy is harnessed as cost-effectively as is possible.

To this end this paper presents numerical investigations of the hydrodynamics of generic marine cross-flow turbines. In contrast to the wind industry, where axial-flow turbines have emerged as the predominant energy converter, a number of different turbine types may yet prove the most cost-effective for energy extraction from tidal flows. Cross-flow turbines offer a number of advantages over more conventional axial-flow turbines. The volume of tidal flow intercepted by a rectangular fronted cross-flow turbine is greater than that intercepted by a circular fronted axial-flow turbine of the same diameter. Hence, cross-flow turbines have greater theoretical potential for energy extraction, both as they intercept a greater energy flux in the undisturbed stream, but also as they present a greater effective blockage and can therefore, when placed in a constrained stream, act to force more flow through the turbine [3]. Furthermore, the modular design distinctive to cross-flow turbines permits the formation of single long turbine arrays, which enable devices to act collectively as barrages with increased performance over that of single devices due to their mutual flow blocking effect. Moreover, such turbine arrays may also allow for a reduction in installation and maintenance costs.

Analytical and small-scale laboratory investigations [4] have revealed that the flow through a cross-flow turbine is extremely complex with simultaneous

attached and separated flow regions as well as reattachment, dynamic stall and blade-vortex interaction events. Hence, numerical modelling of the flow through such turbines necessitates the use of an incompressible viscous flow model that can properly simulate separated flows and account for turbulence effects. Hence, in the present work we choose to use a mesh based Computational Fluid Dynamics (CFD) model. In addition to providing the turbine's torque and power outputs, the CFD model renders a flow-field that can be interrogated to determine vortex structures and blade pressure distributions, and hence permits a detailed analysis of the turbine's flow physics.

It is useful to distinguish between different cross-flow turbine concepts; some cross-flow turbines require additional supporting struts, such as the standard Darrieus turbine [5], whilst other machines are strut free, such as the Gorlov turbine [6] or the Transverse Horizontal Axis Water Turbine (THAWT) [7]. The blades of the latter type are typically supported by end plates. Whilst drag effects associated with supporting struts or end plates will act to reduce turbine power, these effects will be minimised if the turbine blades are long. This paper is particularly concerned with long blade devices such as the THAWT turbine, which uses a truss blade structure to achieve longer unsupported blade lengths. Hence, in the present work the blades are treated as infinitely long and the flow computed as two-dimensional. No account is taken of supporting struts or end plates. Such a flow should be representative of the flow at mid-span of a long bladed turbine.

Non-dimensional analysis shows that aside from blade characteristics; profile, incidence, surface roughness, and incident flow conditions; free-stream profile, turbulence, yaw angle and surface waves, the performance of a cross-flow turbine is governed by six non-dimensional groups; Reynolds number, tip speed ratio, Froude number, blockage ratio, solidity and the number of blades itself. The effects of each of these need to be carefully studied to develop a thorough understanding of the hydrodynamics of cross-flow turbines. This paper explores the dependency of the flow-field and turbine performance on one of the key design variables; turbine solidity. Solidity is defined as the ratio of total blade chord to turbine circumference:

$$\sigma = \frac{cB}{\pi 2R} \qquad (1)$$

where B, c and R are the number of blades, the blade chord length and the turbine radius respectively.

It is evident that solidity can be altered by changing either the turbine radius to blade chord ratio or by changing the number of blades. Here, we choose to alter solidity by changing the number of turbine blades. To this end two turbine configurations with a radius to chord ratio of 16.67 have been investigated. The first turbine examined has two NACA 0015 blades of chord length 0.15m and the second turbine four NACA 0015 blades of the same chord length, resulting in solidities of 0.019 and 0.038 respectively.

Large scale laboratory experiments of several different devices have been conducted, e.g. [7], and it is of interest in developing the understanding of the hydrodynamics of such devices to conduct numerical simulations under similar conditions. Hence, in the present work we choose to simulate flows through turbines at high laboratory Reynolds numbers.

2 Numerical Methods

The simulations presented in this paper have been conducted with the commercial CFD package Fluent [8], which solves the Reynolds-Averaged Navier-Stokes (RANS) equations using a finite volume approach. For this study, Fluent is used as a two-dimensional, segregated, implicit, incompressible flow solver. As the flow problem is unsteady, the evolution of the flow-field is solved on a time marching basis.

The computational domain, a two-dimensional slice orthogonal to the turbine's axis of rotation, is made up of three sub-domains: (i) a far-field domain, (ii) a turbine domain consisting of a circular rotating mesh and (iii) discrete circular domains around each blade. The turbine is of radius R = 16.67 c. The domain extends 8 R upstream and 22 R downstream of the centre of the turbine and 8 R laterally to either side of the turbine. Because the computational domain is two-dimensional, the turbine blades are implicitly assumed to be infinitely long. A consequence of this assumption is that the drag due to the end plates is assumed negligible.

The following boundary conditions were employed in the simulations: (i) no slip condition on the blade surfaces, (ii) unperturbed streamwise flow conditions across the upstream (inflow) and cross-stream boundaries and (iii) a constant pressure condition along the downstream (outflow) boundary. To simulate the rotation of the rotor, the circular turbine mesh with embedded blades is allowed to move relative to the outer inertially fixed domain.

The basic steady flow numerical model was validated by comparing computed lift and drag data for a two-dimensional NACA 0015 aerofoil section over a range of incidences to experimental wind-tunnel data obtained from the Sandia National Laboratories (SNL) [9]. This validation stage enabled the influence of numerical parameters such as mesh resolution, time step, model discretisation and turbulence model, to be investigated. In the present investigation we are interested in high laboratory Reynolds numbers and hence the validation was carried out at a blade Reynolds number $Re_{blade} = 3.6 \times 10^5$, where:

$$Re_{blade} = \frac{cU_\theta}{\nu} \qquad (2)$$

where U_θ and ν are the incident flow velocity and kinematic viscosity respectively (in the case of a rotating turbine this is the blade mean Reynolds number and U_θ is the blade rotational velocity).

During a turbine revolution the blades of a cross-flow turbine may experience large, as well as rapid variations in, angle of incidence, α. Under such conditions the form of the boundary layer cannot be assumed. Hence, the viscous affected inner wall region must be resolved properly in order to enable accurate simulation of the flow within the boundary layer. To this end the performance of two turbulence models with low Re capabilities, Spalart-Allmaras and SST k-ω, were investigated. For proper boundary layer resolution with these models it is desirable that the wall normal resolution is such that $y^+ = O(1)$ for the wall adjacent elements [8], where:

$$y^+ = \frac{\sqrt{\frac{\tau_\omega}{\rho}}\, y}{\nu} \tag{3}$$

where τ_ω, ρ and y are the wall shear stress, fluid density and wall normal distance to the centre of the first cell.

The grid used was a hybrid mesh composed of a very fine structured grid for the near-wall region and unstructured grids for the remainder of the domain, as shown in Fig. 1 & 2. Each hydrofoil surface was modelled with a total of 1492 cells. The first grid spacing from the surface in the normal direction was $1.45 \times 10^{-4}c$, which resulted in $1 < y^+ < 5$ depending on incidence.

Spatial convergence tests identified a mesh size of 94,100 for the circular domain around each blade as optimal with regard to computational costs and a satisfactory degree of convergence of the simulations. This resulted in a total number of elements in the entire turbine domain of 425,000 for the two-bladed and 630,000 for the four-bladed turbine configurations.

As to the model discretisation, the PISO scheme was employed for pressure-velocity coupling, second-order upwind for the momentum equations and first-order upwind for the turbulence modelling equations [8].

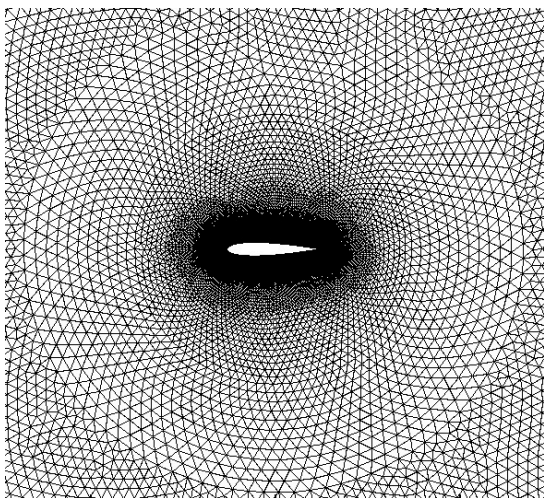A time step of 0.005s was used for all full turbine simulations.
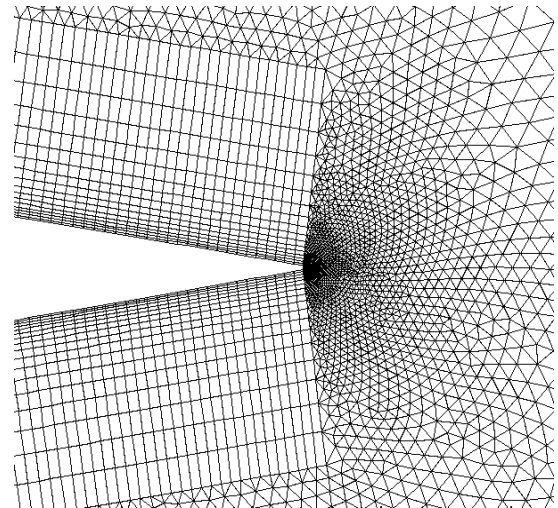

Figure 2: Mesh around a blade's trailing edge

Fig. 3 & 4 show comparisons between the experimental data from static blade tests and our CFD computations using the SST k-ω and Spalart-Allmaras (S-A) turbulence models.

The experimentally derived lift and drag results show the characteristics to be expected for a hydrofoil operating at a moderate Re. At incidences below the static stalling angle, α_{ss}, the coefficient of lift, C_L, increases approximately linearly with α and the coefficient of drag, C_D, is small in comparison to its post stall value. C_L reaches its maximum at around the static stalling angle, while C_D increases significantly at around the same incidence due to the increase in pressure drag caused by flow separation.

Moreover, the SNL tests exhibit the anticipated stalling mechanism. At moderate Reynolds numbers flow separation can occur well below α_{ss} [10]. At low Re, where viscous forces can dampen disturbances that initiate the transition to turbulence, the boundary layer over a hydrofoil blade may be unable to make a natural transition from laminar to turbulent flow and will separate before becoming turbulent. Once separated, however, the separated shear layer may become unstable and undergo transition to turbulence, following which it may reattach to the blade's surface, hence forming a so-called separation bubble. Such bubbles are short at low incidence, but as α increases, the reattachment point moves further downstream and thus the bubble size increases. The formation of such a bubble leads to a sharp increase in drag, whereas its growth rate and hence its effect on lift depend on the Reynolds number [11]. At moderate Reynolds numbers, $10^5 < Re < 2 \times 10^6$, the bubble typically spreads suddenly resulting in a sharp drop in lift, as shown in Fig. 3 for the experimental SNL data.

When examining the results of the numerical simulations, independent of the turbulence model used, three key differences to the experimental data are evident.
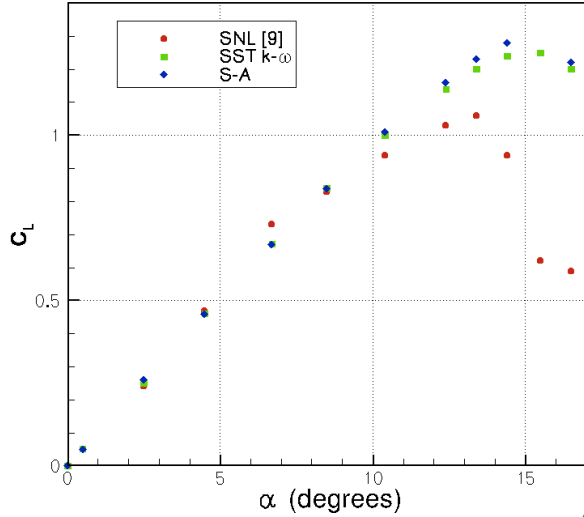

Figure 1: Circular domain around a turbine blade

Figure 3: C_L vs. α for a NACA 0015 blade at Re = 3.6×10^5

Figure 4: C_D vs. α for a NACA 0015 blade at Re = 3.6×10^5

Firstly, as shown in Table 1, C_D for the attached flow region is significantly over-predicted, and, secondly, as highlighted by Fig. 3 & 4, the transition from the attached to the stalled region is poorly simulated; α_{ss} is over-predicted by about 2 degrees and maximum C_L by around 20%.

These deficiencies are due to the difficulty in modelling laminar to turbulent transition using a RANS approach. The few models that can accurately compute transition are not suitable for use in a dynamic flow environment such as that experienced by a cross-flow turbine, whose blades see a continually changing incidence. Existing transition models are of little use and hence the CFD simulations presented here have been computed under fully turbulent flow conditions.

Stipulating the boundary layer to be fully turbulent leads to an over-estimation of the skin friction upstream of where transition would occur in the real flow. As α increases, the real flow transition point moves forward and hence the error in the blade integrated skin friction and thus in blade drag decreases, as shown in Table 1.

α (°)	SST k-w		SA	
	Error_CL	Error_CD	Error_CL	Error_CD
0.5	-4.9%	47.5%	-4.2%	62.1%
2.5	8.2%	44.0%	8.8%	57.3%
4.5	-3.3%	30.7%	-2.9%	41.3%
6.7	-7.4%	18.8%	-7.1%	26.4%
8.5	0.5%	17.1%	1.0%	22.6%
10.4	5.9%	23.0%	7.0%	26.6%
12.4	11.5%	39.9%	13.5%	41.2%

Table 1: Percentage errors in C_L & C_D pre-stall computations

Furthermore, the inability to simulate laminar to turbulent transition is responsible for the differences between the numerical and experimental results of the predictions of stall. Since a fully turbulent boundary layer was assumed throughout, the numerical simulations were in effect modelling a higher Re flow problem which is expected to exhibit a fundamentally different stalling mechanism. As is expected at higher Re, the flow separated from the trailing edge and, as α increased, the point of separation moved upstr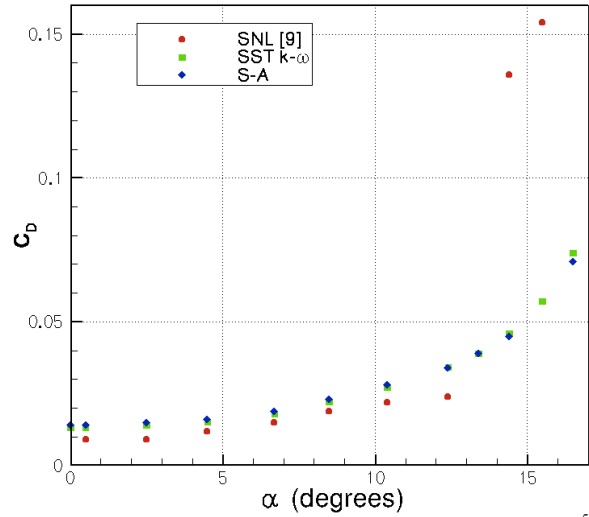eam eventually leading to fully separated flow conditions. In contrast to the stall mechanism at moderate Re, which is governed by a separation bubble, stall initiated at the trailing edge results in a more gradual drop in lift, as can be observed by comparison of the numerical (effective high Re) and experimental (moderate Re) data in Fig. 3.

It is suggested that the effects of separation bubbles and the importance of the laminar to turbulent transition on the hydrofoil's performance will be relatively less important in large scale laboratory and field tests. In reality, free stream turbulence, which can be particularly high in marine currents, may invoke transition to turbulence very close to the blade's leading edge. Hence, the accuracy of this type of CFD simulation should improve as one moves towards simulation of the full scale problem and environment.

Regarding the differences between the simulations using the Spalart-Allmaras and SST k-ω turbulence models, the latter are found to give slightly better force statistics below stall. The numerically computed values of C_L at $\alpha < \alpha_{ss}$ were very similar for both turbulence models, but the average error for C_D at $\alpha < \alpha_{ss}$ was 8% lower for the simulations using the SST k-ω model.

The principal reason why the SST k-ω turbulence model was adopted for the full turbine simulations is linked to the third key difference between the numerical and experimental tests; the results for the post-stall region. The errors in C_L and C_D for $\alpha > \alpha_{ss}$ are significantly larger for the computations using the Spalart-Allmaras model than those when using the SST k-ω model. This behaviour is expected, as the SST k-ω model is more adept at simulating grossly separated flows, see for example [12]. At high angles of attack, $\alpha > 30°$ say, the simulations using the SST k-ω model generated a periodic vortex wake, as might be expected, which was accompanied by periodic blade lift and drag forces (see Fig. 5). In contrast, the Spalart-Allmaras model was unable to simulate a periodic wake flow and the resulting force histories were unrealistically erratic.
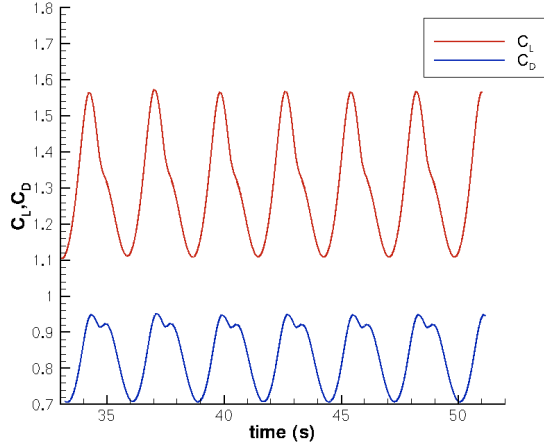
Figure 5: Periodic lift and drag histories for a static blade at $\alpha = 30.8°$ (using the SST k-ω turbulence model)

All simulations presented in the remainder of this paper have been computed using the SST k-ω turbulence model.

3 Results

Having established the choice of numerical parameters for cross-flow turbine simulations at Re = O (10^5) using Fluent, the investigation proceeded to computing the two-dimensional flow-field and turbine performance of a Darrieus-type turbine configuration tested by the SNL [9]:

Number of Blades	2
Hydrofoil	NACA 0015
Chord Length	0.15m
Rotor Radius	2.5m
Solidity	0.019
Rotor Height	5m
Mean Blade Reynolds Number	4.42E+05

Table 2: Turbine parameters

In order to examine the influence of solidity, σ, on turbine performance two turbines were tested. The first with two blades and σ = 0.019, and the second with four blades and σ = 0.038.

Depending on the tip speed ratio, λ, the simulations were run for up to 10 rotor revolutions in order to obtain a statistically converged solution. The tip speed ratio is defined as the ratio of blade speed to free stream flow speed:

$$\lambda = \frac{\omega R}{U_\infty} \tag{4}$$

where ω and U_∞ are the angular and free-stream velocities respectively.

Fig. 6 outlines the fluid mechanical principles of a cross-flow turbine. The circumferentially resolved components of the lift and drag forces are the drivers behind a Darrieus-type turbine, as they combine to give the resultant torque per unit length of blade, T, about the axis of the turbine:

$$T = BR\left(L\sin\alpha - D\cos\alpha\right) \tag{5}$$

where L and D are the sectional lift and drag forces.

The analysis presented in this paper focuses on understanding how the lift generated by each blade varies throughout a cycle and how it may influence turbine performance. Furthermore, we consider how the number of blades influences the cyclic variation of the lift and hence turbine performance. As a first approximation we ignore the contribution made by the drag to the torque and regard torque and lift as somewhat synonymous. This simplification may be justified as $\frac{L\sin\alpha}{D\cos\alpha} \sim O(10)$ for the majority of a turbine revolution. However, we acknowledge that in regions of high drag, such as flow separations, drag plays an important role in determining the instantaneous torque.
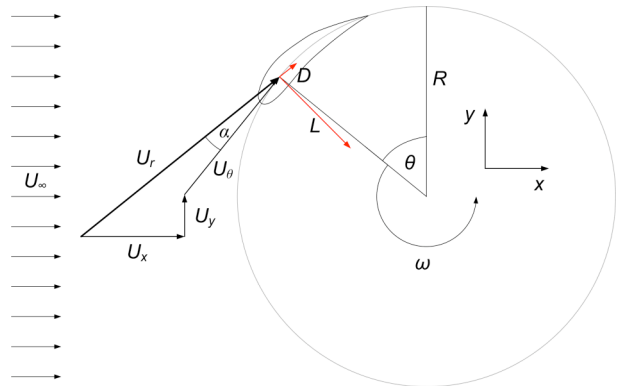

Figure 6: Fluid mechanics of a cross-flow turbine

Careful consideration of the fluid mechanics of cross-flow turbines allows us to elucidate two important observations.

Firstly, a typical power curve for cross-flow turbines has a bell shape, as shown in Fig. 7. This is, as can be deduced from Fig. 6, because at low λ the flow incidence can be high and thus torque and power are limited by blade stalling, whilst the limiting factor at high λ is low lift due to low α; peak power takes place in between, thus leading to a bell shaped power curve.

Secondly, the torque history of a blade for one complete cycle, as shown in Fig. 9 – 11, has two peaks, which correspond to the azimuth positions, θ, where α reaches its maximum pre-stall angle. As evident from Fig. 6, in the absence of blade stall these positions correspond to azimuth angles of θ = 90° and θ = 270°, measured anti-clockwise from the top of the turbine, assuming negligible effects of velocity induction factors. The streamwise velocity induction factor, β, is defined as:

$$\beta = \frac{U_x}{U_{\infty,x}} \tag{6}$$

where $U_x(x,y,t)$ and $U_{\infty,x}$ are the streamwise, i.e. x-direction, components of the velocity and unperturbed free-stream velocity respectively.

On examination of Fig. 9 - 11, the torque peaks are indeed found to lie close to $\theta = 90°$ and $\theta = 270°$. Moreover, a significant difference in the maximum torque, T_{max}, is observed between the upstream and downstream halves of the revolution. The large reduction in T_{max} on the downstream side is due to the streamwise induction factor, β, as further discussed below. In fact, it is the significance of the streamwise induction factor on turbine performance, which renders solidity one of the key design parameters.

The optimum design configuration lies between two extremes; a turbine that presents a very high and a very low impedance. On the one hand, the power output is proportional to the thrust that the turbine exerts on the flow. However, the larger the thrust the larger the flow impedance and hence the lower the flow velocity and energy flux through the turbine. In order that the turbine presents an "efficient" impedance to the flow, the right balance of solidity and tip speed ratio is sought.

This trade-off and the corresponding influence of turbine solidity on turbine performance is discussed in this paper on the basis of the power curves for the two different turbine configurations simulated (see Fig. 7). This figure shows the variation of power coefficient, C_P, against tip speed ratio, where C_P is defined by:

$$C_P = \frac{Power_{mech}}{Power_{kinetic}} = \frac{T\omega}{\frac{1}{2}\rho U_\infty^3 A} \tag{7}$$

where A is the projected frontal area of the turbine per unit length of blade, i.e. A = 2R.

The two- and four-bladed turbines achieve maximum power coefficients of 0.43 and 0.53 respectively.

There are two apparent differences between the forms of the power curves for the different solidities considered. Firstly, the maximum C_P is 23% larger for the four-bladed machine and, secondly, the entire power curve for the higher solidity configuration is shifted to a lower range of tip speed ratios, λ. These differences can be considered with respect to the influence of turbine solidity on the streamwise velocity.

Table 3 shows the spatio-temporal average streamwise velocity induction factor, β, within the circular turbine domain for both turbine configurations at different operating points, λ. The values of β shown in Table 3 were obtained by time averaging spatially averaged flow fields taken at regular intervals through the turbine's periodic cycle.

	$\lambda = 3$	$\lambda = 4$	$\lambda = 8$
$\sigma = 0.019$	0.93	0.87	0.74
$\sigma = 0.038$	0.80	0.73	0.55

Table 3: Average streamwise velocity induction factor, β, within the turbine domain

Table 3 shows that the four-bladed turbine presents a larger impedance, which results in a reduction in streamwise flow velocity between the lower and higher solidity configurations of between 14% and 26% depending on the tip speed ratio. As discussed above, a change in streamwise velocity affects the energy flux through the turbine. In addition it also influences the range of incidences the blades are presented with through the revolution cycle; a lower streamwise induction factor, β, (higher impedance) acts to reduce the maximum angle of incidence.

The effect of β on C_P depends on λ. At high λ, an increase in solidity, σ, and thus decrease in β, results in a decrease in the power take-off, as evident from Fig. 7. This is because at high λ the angle of incidence is low and a decrease in β leads to an even smaller α and hence a reduced lift and torque. Moreover, lift is adversely influenced by the reduction in the resultant velocity, U_r, due to the decrease in the streamwise flow velocity; see Equations 8 & 9.
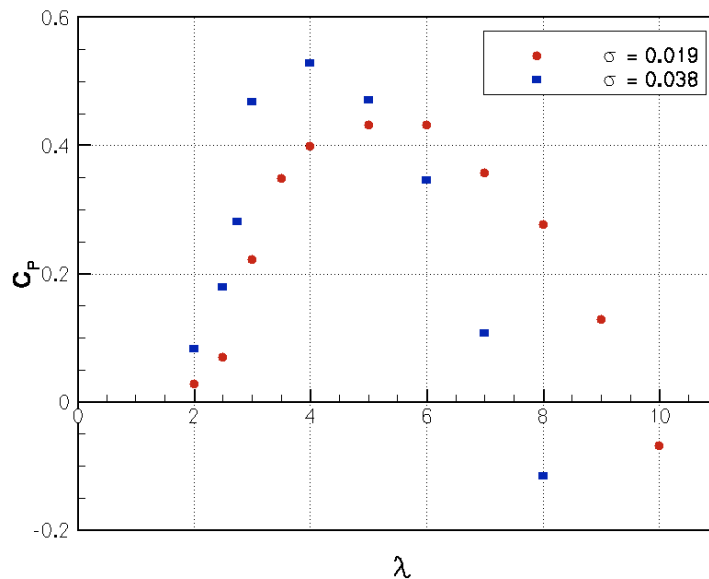

Figure 7: Comparison of C_P vs. λ for two turbines of different solidities

$$L = \frac{1}{2}\rho U_r^2 c C_L \qquad (8)$$

$$U_r = \sqrt{\left(U_x + U_\theta \cos\theta\right)^2 + \left(U_y + U_\theta \sin\theta\right)^2} \qquad (9)$$

where $U_y(x,y,t)$ is the cross-stream, i.e. y-direction, velocity.

This hypothesis is supported by the blade torque histories of the different turbines operating at $\lambda = 8$; see Fig. 11. On the downstream side of the turbine, $180° < \theta < 360°$, where β is lowest, the torque, T, generated by a blade of the higher solidity turbine is less than that of the lower solidity turbine, and is in fact negative.

However, so far only the torque contribution per blade has been considered. Essential with regard to the turbine's performance is whether the deficit in power generated per blade per cycle for the higher solidity turbine is compensated for by the torque provided by the additional blades; Fig. 7 shows that for $\lambda = 8$ the adverse effects of the increase in solidity outweigh the additional torque due to the extra blades, and the higher solidity turbine produces less, in fact negative, power.

At moderate tip speed ratios, $\lambda = 4$ say, the higher solidity turbine exhibits superior performance, as indicated by Fig. 7. However, at these tip speed ratios the individual blades of the lower solidity turbine generate a higher net torque per blade, as evident from Fig. 10. This is because at $\lambda = 4$ the flow over the blades of the lower solidity turbine remains attached (as compared to lower tip speed ratios; see discussion below) and hence increasing solidity reduces overall lift through reduced streamwise velocity and hence reduced incidence and resultant flow velocity. Fig. 8 shows a plot of instantaneous streamlines for a blade of the two-bladed turbine at $\theta = 91°$, close to where the hydrofoil experiences maximum incidence; it is clearly evident that the flow over the blade remains fully attached.

In contrast to higher tip speed ratios, at $\lambda = 4$ the additional torque provided by the additional blades of the higher solidity device offsets the reduction in net torque per blade such that at $\lambda = 4$ the higher solidity device yields more power.

At lower tip speed ratios, increasing solidity may further increase the turbine's power take-off relative to the lower solidity device; for instance at $\lambda = 3$ the four-bladed turbine generates 113% more power than the two-bladed device. This is because a lower solidity device may experience significant stall at low λ, whilst a higher solidity turbine may not due to decreased streamwise velocity. This is illustrated in terms of torque in Fig. 9, in which it is seen that the blade torque of the lower solidity turbine experiences significant fluctuations, which are associated with large scale vortex shedding that occur as a result of flow separation. The net result is that there is little change in net torque per cycle per blade between the two turbine configurations, but an increase in total turbine torque for the higher solidity device as there are more blades.
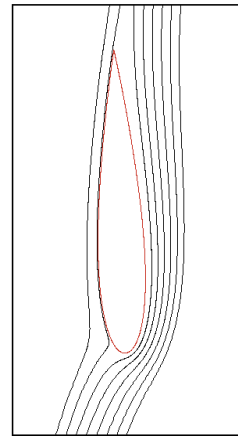

Figure 8: Streamline plot for $\lambda = 4$, B = 2, $\theta = 91°$

The differences between the two turbine configurations at low tip speed ratios are underlined by comparison of instantaneous streamline plots.

Fig.12 shows streamline plots for the two-bladed turbine operating at $\lambda = 3$ for four different blade azimuth positions over the upstream half of the turbine. It is evident that the blades of the lower solidity turbine operate under stalled conditions for $\theta > 90°$, which explains the low blade torque generated between $\theta = 110° - 160°$; see Fig. 9. The flow is observed to reattach at around $\theta = 160°$.
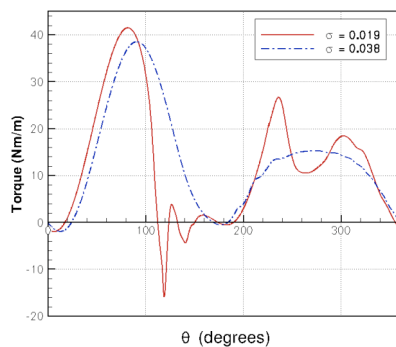

Figure 9: $\lambda = 3$: Torque history of a blade starting at $\theta = 0°$
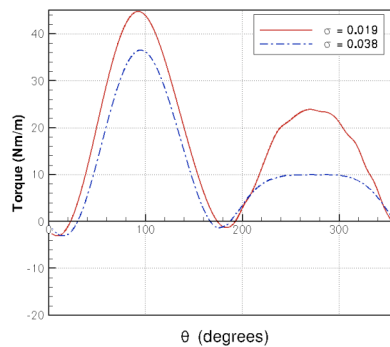

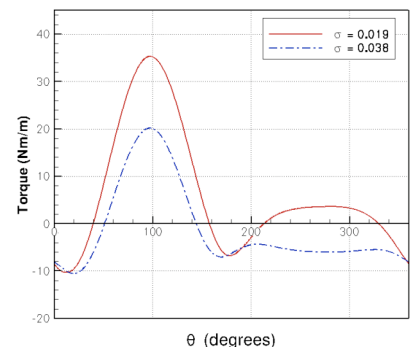**Figure 10:** $\lambda = 4$: Torque history of a blade starting at $\theta = 0°$

Figure 11: $\lambda = 8$: Torque history of a blade starting at $\theta = 0°$

490
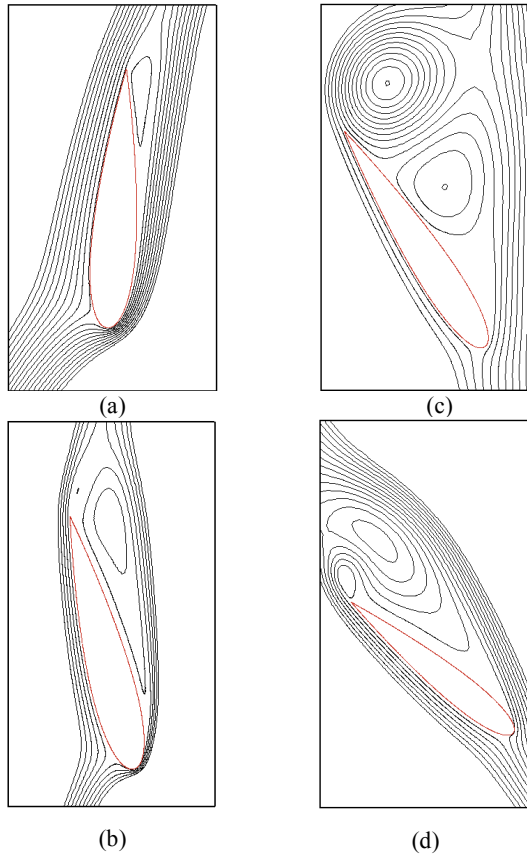
Figure 12: Streamline plots for $\lambda = 3$, B = 2, $\theta = 86°$, 104°, 122°, 140° (a-d)

Figure 13: Streamline plots for $\lambda = 3$, B = 4, $\theta = 108°$, 126°, 144°, 162° (a-d)

Fig. 13 shows streamline plots for the four-bladed turbine operating at $\lambda = 3$ for four different blade positions over the upstream half of the turbine. It is apparent that the flow over the blades of the higher solidity turbine starts to separate at the trailing edge, and that the point of separation moves towards the leading edge with increasing azimuth angle. However, unlike the lower solidity device, the four-bladed turbine's blades do not undergo gross scale vortex shedding. Hence, the four-bladed turbine exhibits superior performance for $\theta = 110°$ - 160°.

The torque maximum, T_{max}, on the upstream half of the two-bladed turbine occurs at a lower azimuth angle, θ, than might be expected due to flow separation. For the higher solidity device the reduction in streamwise velocity results in lower flow incidences and the static stall angle, α_{ss}, is not reached until a higher azimuth angle. Hence, T_{max} on the upstream side occurs at higher θ for the higher solidity device.
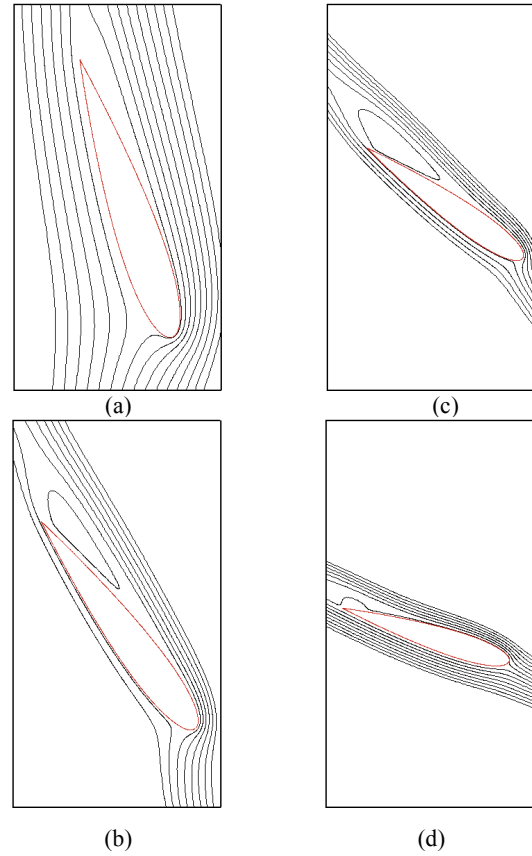
Fig. 14 shows a comparison of the net (all blades) torque histories for the two turbines when operating at a tip speed ratio of 4. The lower and higher solidity turbines achieve mean torques (per unit length of blade) of 31.8 N and 44.8 N respectively. This results in the significant difference in the corresponding C_P values at $\lambda = 4$ apparent in Fig. 7.
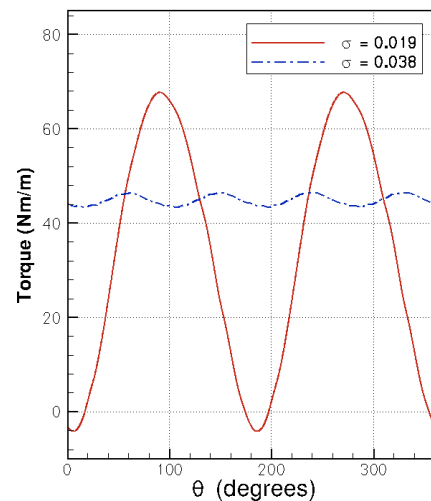

Figure 14: Comparison of full turbine torque history at $\lambda = 4$

The key observation from Fig. 14 is the considerably more even loading experienced by the four-bladed turbine, which is a particularly favourably characteristic with regard to generator loading and fatigue issues. Aside from the turbine's performance and its cost, which will partly depend on its solidity, turbine fatigue characteristics are important in identifying optimal turbine designs.

On the downstream side of the turbine, the flow over the blades of the lower solidity turbine was observed to separate from the blade's trailing edge at around $\theta = 240°$ and a large vortex structure formed by $\theta = 266°$; see Fig. 15.
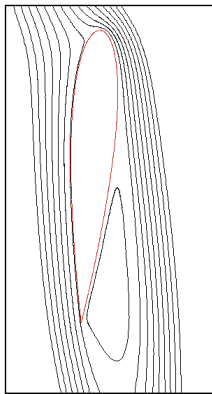

Figure 15: $\lambda = 3$: Streamline plot for $\lambda = 3$, B = 2, $\theta = 266°$

However, despite the extensive region of separated flow the hydrofoil of the two-bladed turbine generated significantly higher torque than its four bladed-counterpart between $\theta = 210°$ & $330°$; see Fig. 9. The torque peaks observed for the two-bladed turbine on the downstream side are a result of increased lift force on

blades operating beyond static stall conditions and are therefore a result of dynamic stall.

Static stall, which ought to occur at around $\alpha = 14°$, is exceeded by about 5°, and the blades experience lift force hystereses, typical of dynamic stall. Fig. 16 & 17 show the sectional lift and drag forces experienced by a single blade of the two-bladed turbine at $\lambda = 3$ as it traverses a full rotation cycle. In the manner plotted, positive incidence refers to the downstream pass of the blade, whilst negative incidence refers to the upstream blade pass. Examining the blade's C_L variation, it is evident that the blade experiences dynamic stall on both the upstream and downstream sides of the turbine, similar to dynamic stall events reported in [13-15].

It is interesting to note the different effect of dynamic stall on the upstream and downstream sides of the turbine. As the maximum incidence, once velocity induction effects are taken in to account, is higher on the upstream side of the turbine than on the downstream side, the adverse effects of the hysteresis loop are more significant for $0° < \theta < 180°$, as evident in Fig. 9. It is clear that on the upstream side of the turbine, there is large scale vortex shedding resulting in a large increase in sectional drag and an unsteady lift behaviour with respect to incidence. Note also that on the downstream side of the turbine there are two local peaks in C_L, one as α increases and the other as α decreases. These peaks correspond to the local torque maxima at $\theta = 230°$ and $300°$. Despite the superior performance on the downstream side of the turbine the net effect of dynamic stall at this solidity and tip speed ratio is negative due to the poor performance on the upstream side of the turbine.
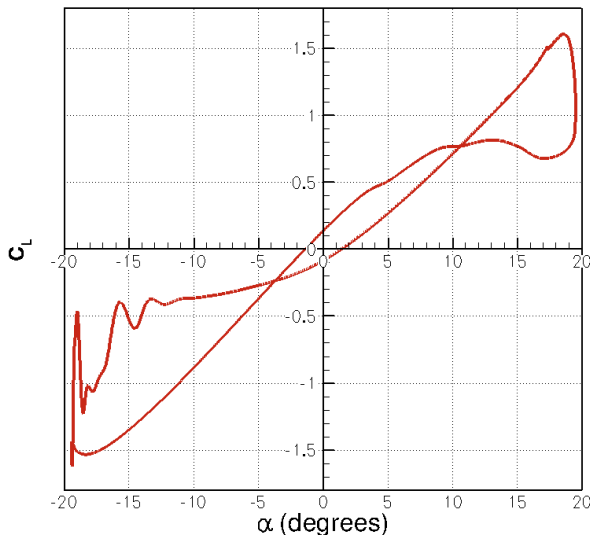

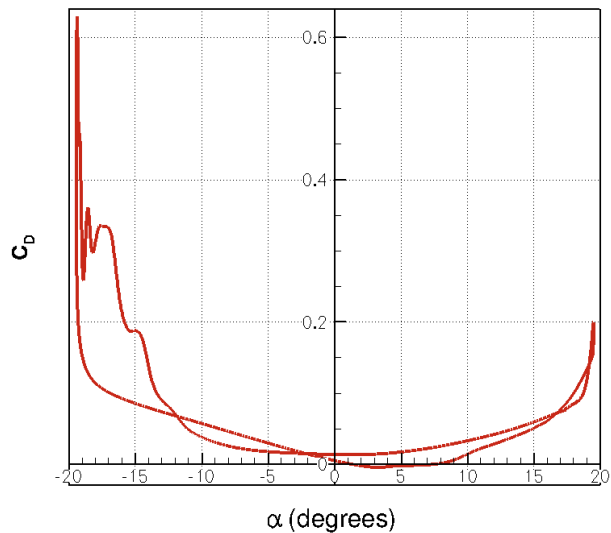**Figure 16:** C_L history for a blade of the 2-bladed turbine

Figure 17: C_D history for a blade of the 2-bladed turbine

4 Conclusion

A two-dimensional RANS based CFD model has been used to compare the performances of a two-bladed and a four-bladed cross-flow turbine, with solidities of 0.019 & 0.038 respectively, operating at an average blade Reynolds number of 4.42×10^5.

The numerical investigations showed that increasing the number of blades from two to four resulted in an increase in the maximum power coefficient from 0.43 to 0.53. However, no account has been taken of drag penalties resulting from additional blade support struts.

Furthermore, increasing the number of blades resulted in a reduction in the spatio-temporal mean streamwise flow velocity within the turbine of between 14% and 26% depending on the tip speed ratio. Due to the decrease in streamwise velocity the blades of the higher solidity turbine were presented with lower angles of attack, which resulted in the entire power curve being shifted to lower tip speed ratios. At low tip speed ratios, power take-off is limited by stalling, so that a decrease in the angle of attack, due to higher solidity, results in an increase in lift and hence power generated, whilst at high tip speed ratios, low angles of attack are the limiting factor, so that a decrease in the angle of attack due to higher solidity results in lower lift and thus power.

At a tip speed ratio of 3 dynamic stall was observed to occur for the lower solidity turbine on both the upstream and downstream blade passes. In this instance the net effect of dynamic stall on turbine performance was shown to be negative.

Acknowledgements

References

[1] Savage A. Tidal Power in the UK - Tidal technologies overview. Sustainable Development Commission 2007.

[2] BERR. Energy Consumption in the United Kingdom 2008.

[3] Whelan JI, Graham JMR, Peiro J. A free-surface and blockage correction for tidal turbines. Journal of Fluid Mechanics 2009;624:281-91.

[4] Consul CA. Hydrodynamic Analysis and Design Optimisation of a Marine Tidal Cross-Flow Turbine. University of Oxford 2008.

[5] Shiono M, Suzuki K, Kiho S. Experimental study of the characteristics of a Darrieus turbine for tidal power generation. Electrical Engineering in Japan 2000;132(3):38-47.

[6] Gorlov AM. The Helical Turbine and its applications for tidal and wave power. OCEANS 2003. Proceedings, 2003. p. 1996 Vol.4.

[7] McAdam RA, Houlsby GT, Oldfield MLG, McCulloch MD. Experimental Testing of the Transverse Horizontal Axis Water Turbine. 8th European Wave and Tidal Energy Conference Uppsala, Sweden, 2009.

[8] Ansys. The Fluent Manuel, 2008.

[9] Sheldahl RE, Klimas PC. Aerodynamic Characteristics of Seven Symmetrical Airfoil Sections Through 180-Degree Angle of Attack for Use in Aerodynamic Analysis of Vertical Axis Wind Turbines. Sandia National Laboratories 1981.

[10] Mayda EA, van Dam CP. Bubble-induced unsteadiness on a wind turbine airfoil. Transactions of the ASME. Journal of Solar Energy Engineering 2002;124(4):335-44.

[11] Sharpe DJ. Wind Turbine Aerodynamics In: Freris LL Wind Energy Conversion Systems Prentice Hall, 1990.

[12] Tucker PG. Turbulence modelling of problem aerospace flows. International Journal for Numerical Methods in Fluids 2006;51(3):261-83.

[13] McCroskey WJ. The Phenomenon of Dynamic Stall. NASA Technical Memorandum 81624 1981.

[14] Carr LW. Progress in Analysis and Prediction of Dynamic Stall. Journal of Aircraft 1988;25(1):6-17.

[15] Tang DM, Dowell EH. Experimental investigation of three-dimensional dynamic stall model oscillating in pitch. Journal of Aircraft 1995;32(5):1062-71.